2-20-2009

Aglite Lidar: A Portable Elastic Lidar System for Investivating Aerosol and Wind Motions at or Around Agricultural Production Facilities

Christian C. Marchant
Utah State University

Thomas D. Wilkerson

Gail E. Bingham

Vladimir V. Zavyalov

Jan Marie Andersen

Cordell B. Wright

See next page for additional authors

Recommended Citation

Marchant, Christian C.; Wilkerson, Thomas D.; Bingham, Gail E.; Zavyalov, Vladimir V.; Andersen, Jan Marie; Wright, Cordell B.; Cornelsen, Scott S.; Cornelsen, Randal S.; Silva, Philip J.; and Hatfield, Jerry L., "Aglite Lidar: A Portable Elastic Lidar System for Investivating Aerosol and Wind Motions at or Around Agricultural Production Facilities" (2009). *Space Dynamics Laboratory Publications.* Paper 84.
https://digitalcommons.usu.edu/sdl_pubs/84

Authors

Christian C. Marchant, Thomas D. Wilkerson, Gail E. Bingham, Vladimir V. Zavyalov, Jan Marie Andersen, Cordell B. Wright, Scott S. Cornelsen, Randal S. Cornelsen, Philip J. Silva, and Jerry L. Hatfield

Journal of Applied Remote Sensing, Vol. 3, 033511 (20 February 2009)

Aglite lidar: a portable elastic lidar system for investigating aerosol and wind motions at or around agricultural production facilities

Christian C. Marchant[1], Thomas D. Wilkerson[1], Gail E. Bingham[1], Vladimir V. Zavyalov[1], Jan Marie Andersen[1], Cordell B. Wright[1], Scott S. Cornelsen[2], Randal S. Martin[3], Philip J. Silva[3], Jerry L. Hatfield[4]
[1]Space Dynamics Laboratory, 1695 North Research Parkway, North Logan, UT 84341
Tel: 435-797-9611 Fax: 435-797-4599, tom.wilkerson@sdl.usu.edu
[2]Campbell Scientific, Logan, UT 84341
[3]Utah State University, Logan, UT 84322
[4]Agricultural Research Service, National Soil Tilth Laboratory, 2110 University Blvd., Ames, IA 50011-4420, jerry.hatfield@ars.usda.gov

Abstract. The Aglite Lidar is a portable scanning lidar that can be quickly deployed at agricultural and other air quality study sites. The purpose of Aglite is to map the concentration of PM_{10} and $PM_{2.5}$ in aerosol plumes from agricultural and other sources. Aglite uses a high-repetition rate low-pulse energy 3-wavelength YAG laser with photon-counting detection together with a steerable pointing mirror to measure aerosol concentration with high spatial and temporal resolution. Aglite has been used in field campaigns in Iowa, Utah and California. The instrument is described, and performance and lidar sensitivity data are presented. The value of the lidar in aerosol plume mapping is demonstrated, as is the ability to extract wind-speed information from the lidar data

Keywords: lidar, aerosol, wind motion, PM_{10}, $PM_{2.5}$

1 INTRODUCTION

Agricultural aerosol sources can contribute a significant component to air pollution in many regions of the country. Characterization of the aerosol emissions of agricultural operations is required to determine best management practices for controlling agricultural aerosol emissions and to establish a scientific basis for crafting regulations concerning agricultural aerosols. For regulatory purposes, aerosol mass concentration is measured in terms of PM_{10} and $PM_{2.5}$, both of which are pollutants regulated by the National Ambient Air Quality Standards [1][2].

Examples of agricultural sources of PM_{10} and $PM_{2.5}$ include “fugitive dust” from soil tillage, aerosols generated from crop processing, and chemical precipitate from vapors emitted by manure. An agricultural aerosol source differs from industrial aerosol sources in that the source is often spread out over a significant area, resulting in a highly dispersed aerosol plume and a variation in the rate of emission over time.

In the past, conventional methods for measuring and characterizing aerosol sources have used point sensors and software models of atmospheric dispersion. Using these tools, measurements are made by deploying a limited number of point sensor instruments around the site of interest and using software models to interpolate and extrapolate aerosol concentration values around the entire site. These methods offer low spatial resolution due to the sparse number of instruments. Additionally, these methods rely on assumptions of Gaussian diffusion of aerosols and are therefore reliable only over relatively long periods of time. Attempts have also been made to measure emissions from soil tillage operations by placing instruments directly on a tractor implement [3][4][5][6].

[DOI: 10.1117/1.3097928]
Received 4 Aug 2008; accepted 17 Feb 2009; published 20 Feb 2009 [CCC: 19313195/2009/$25.00]

The deficiency of these conventional techniques is that they are unable to make measurements over the volume of a dispersed aerosol plume. A sparse distribution of instruments is unable to cover the entire area of the aerosol source, and the point sensors cannot take measurements higher than the towers upon which they are mounted. As a result, these techniques are insufficient for characterizing the emission rate of the whole plume.

This deficiency can be addressed using lidar technology, which provides a means to measure the distribution of aerosols over large areas with high spatial and temporal resolution. Previous applications of lidar technology to measuring agricultural aerosols have demonstrated this capability by measuring the height and morphology of dust plumes generated by field preparation [7][8]. Mapping of aerosol concentration by lidar has been demonstrated in agricultural settings [9][10]. The interaction of lidar scan patterns and moving aerosols provides valuable information on the wind structures responsible for aerosol transport. In particular, certain types of scans permit the visualization of wind velocity, variability of wind speed over large areas, and shapes of aerosol plumes. Buttler et al. (2001) reviewed lidar wind velocity measurements, principally those based on cross-correlations between successive positions of aerosol clouds, with the lidar direction oriented along the wind or cross-wind. They compared wind data collected with radiosondes, remote laser Doppler profiles, and elastic backscatter lidar profiles. Good agreements were demonstrated between these instruments, indicating that wind observations with elastic lidar afford valuable data on the transport within the planetary boundary layer [11]. Kovalev and Eichinger (2004) provide a comprehensive review of backscatter correlation methods and Doppler-based lidar techniques in both the time and frequency domains, and point out (pp. 507-8) the many types of atmospheric observations in which wind lidar technology can now play an important role [12]. Pioneering work on correlations was carried out by Derr and Little (1970), Zuev (1973), and Eloranta (1975) [13][14][15]. Sasano et al. (1982) corrected the 2D aerosol patterns for their motion during the lidar scan, and found that the correlation-based wind velocities agreed with the wind data from co-located meteorology towers [16].

Three-dimensional, volume-imaging scans have been developed for wind profile measurements [17][18][19]. The lofting of aerosol plumes from a farm due to a combination of wind and convection has been shown by Eichinger (2006) [20]. The development of holographic scanning lidars by Schwemmer (1993), Guerra et al. (1999), Schwemmer et al. (2001), Wilkerson et al. (2003) and Wilkerson et al. (2005) has led to new methods of cross-beam wind analysis using aerosol and cloud tracking [21][22][23][24][25]. The work reported here is based on simple, straightforward analyses of (1) one-dimensional plume motion as a function of time and (2) the visualization of two-dimensional plumes by time-dependent lidar scans across the plume shape.

The Space Dynamics Laboratory (SDL) at Utah State University teamed with researchers from the Department of Agriculture, Agriculture Research Service (ARS) to build Aglite, a system of an elastic lidar plus an array of point source instruments and software for measuring the emission rate of agricultural aerosol sources. In addition to measuring the 3-dimensional structure of an agricultural aerosol plume over a large volume, the Aglite system is able measure the concentration of $PM_{2.5}$ and PM_{10}. These data are used in conjunction with data on wind speed and direction to characterize the emission rate of the source, as described by Bingham et al. [26].

Here we describe the design of the Aglite lidar and demonstrate its ability to map the aerosol concentration and dynamics of aerosol plumes with high resolution. We also demonstrate Aglite's ability to measure wind velocity by means of aerosol tracking.

2 AGLITE LIDAR DESCRIPTION

The primary system requirements of the Aglite lidar were to (1) make the system eye-safe at the operating range; (2) make the system sufficiently robust and portable to be deployed at an agricultural site, and (3) make the scanning and data logging sufficiently fast to capture the dynamics and structure of an entire plume.

The Aglite instrument is a portable lidar mounted in a small trailer and utilizing a fixed vertical telescope with a steering mirror used as an azimuth-elevation beam director. The lidar has a measurement rate as fast as 1/10 of a second, with a minimum of 6 m range resolution and 3 km analysis range. Aglite's steering mirror and fast response time enable it to map aerosol concentration in units of $PM_{2.5}$ and PM_{10} over a large volume of air in a relatively short amount of time, with a single 2-dimensional scan taking less than a minute. This speed also enables Aglite to capture plume dynamics with good temporal resolution.

2.1 Aglite Lidar Design

The requirement to make Aglite eye-safe drove the decision to make Aglite a micropulse lidar. This mitigates eye-safety issues because of the lower pulse energy. Additionally, the high pulse rate potentially allows for an extremely high measurement rate. As a consequence of the low pulse-energy, photon-counting detection is used. The lidar has a narrow field of view (FOV) and uses narrow-band filters to limit background noise from solar radiation. The design concepts for Aglite and its component layout are shown in Fig. 1A and B, and are based in part on the design by McGill et al. (2002) for the Cloud Physics Lidar [27].

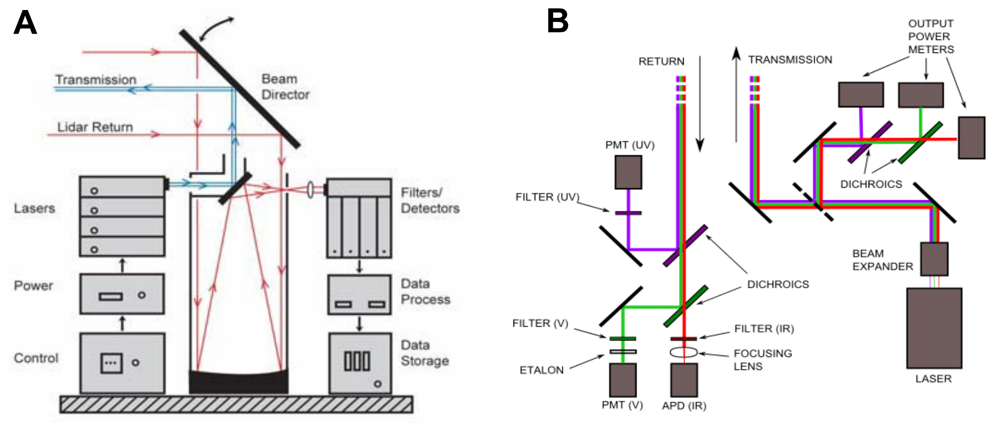

Fig. 1. (A) The Aglite lidar conceptual arrangement. (B) The physical layout of the optical components on the optical bench.

The transmitter chosen for Aglite is a solid-state Nd:YAG laser from Photonics Industries International, Inc. (Photonics Industries International, Inc, 390 Central Avenue, Bohemia, NY 11716). (The instruments and manufacturers named herein were used in the research experiments described; however, their use does not constitute an endorsement or preferential treatment by the researchers or the project sponsors.) The laser generates three wavelengths: 1064, 532, and 355 nm using doubling and tripling crystals. The laser operates at 10 KHz and is diode-pumped. The laser head is vertically mounted on the optical bench of the lidar and is coupled to the diodes and the power supply, which are located in the electronics rack. The laser is water-cooled and is coupled to a separate chiller. Immediately after leaving the laser head, the beam passes first through a 7x beam expander, at which point the beam far-field full divergence angles are 0.37, 0.30, and 0.27 mrad respectively. Average output powers employed are 4.35, 0.48, and 0.93 W respectively, yielding pulse energies of 435, 50, and 93 μJ.

The beam is directed through a neutral density (ND) filter station, which allows for controlled attenuation of the beam (20 to 100% power) as desired over the lidar's operating range on grounds of eye safety. Reflection from the ND filter is separated into its component wavelengths using dichroic reflectors and fed into power sensors to monitor laser output strength, as shown in Fig. 1B. After passing through the ND filter, the beam is directed onto a mirror mounted on the central obstruction of the telescope, at which point the laser is co-aligned with the receiver telescope.

Aglite uses a simple Newtonian telescope with a 28-cm diameter primary mirror (Fig. 1A). The mirror has a focal length of 0.91 meters. A field stop confines the telescope's full field-of-view to 0.45 mrad. After the laser beam reflects off the telescope's central obstruction, a pointing mirror directs the beam and collects the returned signal. At this point, the outgoing beam and returned signal are coaxially aligned. Movement of the pointing mirror controls the direction the lidar looks, but does not change the relative alignment of the outgoing beam and return signal. The pointing mirror actuators have a pointing knowledge resolution of 1 mrad and pointing repeatability of 5 mrad.

As shown in Fig. 1B, the signal is collected by the telescope and separated into its component wavelengths using dichroics. Each channel then passes through a narrow-band interference filter made by Barr Associates, Inc. (Barr Associates, Inc, 2 Lyberty Way, Westford, Massachusetts 01886.) The 532 nm channel then passes through an etalon made by TecOptics (TecOptics, 1760 Grand Avenue, Merrick, NY 11566.) The 1064 nm channel is focused onto an avalanche photo-diode (APD), while the remaining two channels pass into photo-multiplier tubes (PMT). The APD is model SPCM-AQR-14 made by PerkinElmer (PerkinElmer, 44370 Christy Street, Fremont, California 94538), having a quantum efficiency of 2%. The PMTs are model 9954A made by Electron Tubes (Electron Tubes, 100 Forge Way, Unit F, Rockaway, New Jersey 07866), with quantum efficiencies of 14% and 27% at 532 and 355 nm respectively. The choice of detectors for Aglite was based on the generally superior signal-to-noise ratio for PMTs in the visible and ultraviolet wavelengths, given sufficient filtering of the green intensity maximum of sunlight, and the infrared sensitivity of the APD. This conclusion has also been confirmed by Agishev et al. (2006) [28]. A commercial high speed, multichannel photon counting interface (APCS, ASRC Aerospace, Greenbelt, MD) was used to log and record the photon counts for each channel. The electronic system for operating the entire Aglite system and recording the multichannel data has been described in detail by Cornelsen (2005) [29].

For example, the Fabry-Perot (FP) etalon inside Aglite on the 532nm channel is not temperature controlled, as is sometimes done in lidar instrumentation. The Aglite system compensates for temperature induced instrument changes by periodic (every 20 min) recalibration of the lidar return signal magnitude against an OPC placed in the field. It is important that the instrument not fluctuate during the course of a single 20 min scan. The etalon discussed here is an air spaced etalon constructed of Class 0 Zerodur with a nominal mirror spacing of 4.011 mm. The coefficient of thermal expansion of Zerodur is 0.002 ppm/K. During a typical 10-hour day of field experiments, the temperature inside of the lidar enclosure can change as much as 25 K, corresponding to an etalon spacing change of 0.5 ppm, or 2 nm. The transmission change due to a 2-nm spacing increase is < 1%, and the peak shift of the transmission fringe is < 0.25 pm. Therefore the transmission changes over any given 20-minute scan are limited to temperature effects of a single Kelvin or less, and so are on the order of 0.05% transmission changes. Either way, the transmission changes due to temperature effects are well within the 37 pm bandwidth of the etalon and also that of the laser. Therefore, systematic temperature induced transmission changes do not contribute significantly to the observed noise threshold for the entire instrument.

The actual range resolution of this lidar lies in the range of 12-18 m for wavelengths between 355 and 1064 nm, owing to the data system's time bins of 40 nsec, the respective laser pulse lengths, and the pulse discrimination times of the detectors. The repetition rate of the laser sets the lidar's maximum range at 15 km; in practice, the maximum useful range can be as close as 1.5 km due to high solar background radiation and/or unfavorable atmospheric conditions.

The laser head, transmission optics, and receiver optics are all mounted on a single optical bench, vertically oriented in a 6-point vibration-isolated frame along with the telescope. The optical path is housed under light-tight aluminum covers that also serve to keep the optics clean. The entire frame is covered with removable panels. An important component of the lidar is an external air-blower. This draws air from outside of the trailer through a filter, conditions it, and blows it into the lidar housing to maintain positive pressure in the optical system and minimize flying insect intrusion. This is essential to mitigate the risks of contamination from dust and insects during a campaign because the receiver telescope is exposed to the outside environment.

The beam director is computer controlled by a rack-mounted PC, with scan control points established using the visible camera and a game controller. Azimuth and elevation control were achieved using Newport RV series and BG series precision motorized stages. It can traverse the beam 270° in the horizontal and +45° to -10° in the vertical, and is retracted hydraulically inside the trailer for travel. A video camera looks at the director mirror to provide the operator a 5° field of view along the beam path for safety monitoring. Data from the lidar can be linked by WiFi network to other sites and bring environmental data to the operator. Table 1 summarizes the system parameters of the lidar.

Table 1. Aglite lidar system parameters

Laser/Telescope		**Detectors/Bandwidths**	
Wavelengths	1064, 532, and 355 nm	Effective filter bandwidth	150 pm at 1064 nm
Laser type	Solid-state Nd:YAG	(full width, half-height)	120 pm at 532 nm
			150 pm at 355 nm
Laser repetition rate	10 kHz	Filter efficiency	70% at 1064 nm 70% at 532 nm 76% at 355 nm
Laser output energy	435 μJ at 1064 nm 50 μJ at 532 nm 93 μJ at 355 nm	Etalon free spectral range	37 pm at 532 nm
Telescope diameter	28 cm	Etalon reflectivity finesse	6.1 at 532 nm
Telescope type	Newtonian	Etalon peak transmission	> 98.4% at 532 nm
Telescope FOV	450 μrad, full angle	Detector photon counting efficiency	2% at 1064 nm 14% at 532 nm 27% at 355 nm
Resolutions			
Data time resolution	0.1 sec possible; typical 1-3 s.		
Data range resolution	18 m at 1064 nm 12 m at 532 nm 12 m at 355 nm		
Steering resolution	5 μrad		

2.2 Lidar Eye-Safety

For safe field operation the lidar beam should be eye-safe at the facility under investigation, and the intervening area should be guaranteed off limits to personnel. The most demanding eye-safety criterion for Aglite is the green light at 532 nm near the peak sensitivity of the human eye. While certain other lidar groups have preferred to operate at “eye safe” infrared wavelengths such as 1555 nm (e.g. Gong et al., 2007, [30]), the Nd:YAG-derived triplet (355, 532, 1064 nm) was chosen for Aglite on the basis of good control over the field test environment and the three wavelength capability for discriminating between aerosol types. For Aglite the requirement is that the operating distance of the lidar from the facility must meet or exceed the eye-safety range for 532 nm, which is approximately 450 meters using 20% of the laser power. Calculations of the value of the Nominal Optical Hazard Distance, R_{NOHD}, for eye exposure are carried out in accordance with ANSI Laser Safety Standard Z136.1 [31]. The ophthalmic basis for these standards has most recently been treated by Delori, Webb and Sliney (2007) [32].

The minimum distance for safe eye exposure to *N* laser pulses at a given wavelength is

$$R_{NOHD}(cm) = (1/\theta)\cdot[4\Phi/\pi\cdot MPE(N)]^{1/2}, \tag{1}$$

where θ is the full divergence angle of the transmitted laser pulse (mrad), Φ is the pulse energy (*J*), and $MPE(N) = (MPE_P)\cdot N^{-1/4}$, where MPE_P is the Maximum Permissible Exposure per pulse (J/cm^2) at the human cornea for each wavelength. Table 2 provides representative values for R_{NOHD} for the range of laser output powers of Aglite, based on a standard blink response criterion of 0.25 seconds. At an operating distance of 600 meters and reduced optical power, Aglite is “eye-safe” at all wavelengths. The equivalent ranges for other exposure durations are readily calculated using recognized standards [31][33][34]. Table 2 shows a conservative analysis of eye-safety distances based on 100% optical efficiency of laser transmission.

Table 2. Representative eye-safety distances for Aglite lidar for “blink” exposure of ¼ second at laser PRF of 10 kHz

λ (nm)	MPE_P (J/cm^2)	Φ(μJ)	R_{NOHD}(meters) @ 20% output	R_{NOHD}(meters) @ 100% output
355	5.6 E(-3)	100	6.7	15
532	5.0 E(-7)	50	450	1000
1064	5.0 E(-6)	500	360	810

3 LIDAR DATA AND CALIBRATION

The information content of the lidar return is summarized by the well-known lidar equation (2), which describes the lidar return signal as a function of range z for wavelength λ:

$$P_\lambda(z) = P_0 \cdot L \cdot \frac{c\tau}{2} \cdot A_\lambda(z) \cdot \frac{\beta_\lambda(z)}{z^2} \cdot \exp\left(-2\int_0^z \sigma_\lambda(z')\partial z'\right). \tag{2}$$

The term $P_\lambda(z)$ is the measured reflected power for distance *z* and is measured in photon counts. P_0 is the output power of the lidar, *L* is the lidar coefficient, which represents system efficiency, *c* is the speed of light, τ is the pulse width of the lidar and $A_\lambda(z)$ is the effective area of the receiving telescope. $A_\lambda(z)$= GFF$\cdot A$, where *A* is the geometric area of the telescope and GFF is a geometric form factor or overlap function defined by the geometry of the transmitter and telescope. $\beta_\lambda(z)$ is the atmospheric backscatter coefficient, and $\sigma_\lambda(z)$ is the atmospheric extinction coefficient.

The backscatter and extinction coefficients both depend upon molecular scattering, as well as on the characteristics of the background and emission aerosols. The solution of (2) requires knowledge of the optical parameters of both the background and source aerosols, as well as the contribution of molecular scattering; these need to be measured at one or more reference points in order to interpret lidar return intensity in terms of particle concentration, and to extract aerosol information [35].

The magnitude and shape of the geometric form factor (GFF) is highly sensitive to the alignment of the lidar optics. The expected value of the GFF is approximately 80% at the lidar range of 650 m (Fig. 2), as modeled using the optical design parameters of the lidar [36]. Experimentally derived values for the GFF were found to be within 10% of the modeled GFF for ranges greater than 650 m [37]. Because of the GFF's sensitivity of the GFF to misalignment of the optics, the lidar system is aligned before measurements are taken. This is done using a target at distances greater than 1 km; the lidar is directed at the target, and the optics are adjusted to maximize the magnitude of the signal reflected by the target.

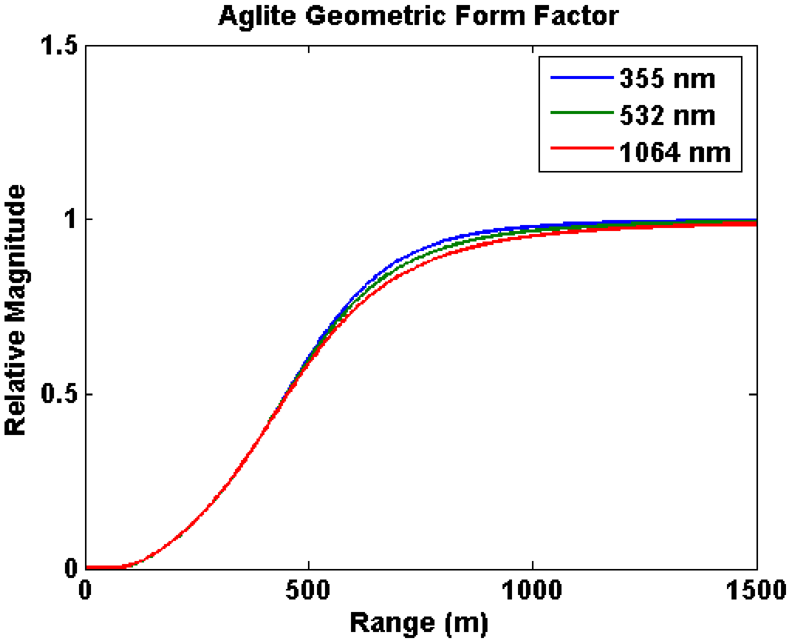

Fig. 2. The Aglite geometric form factor, or collection efficiency function, shown as a function of distance from the transmitter.

To calibrate the aerosol density detected by Aglite, we determined the local particulate concentrations in the lidar's FOV using both optical and aerodynamic mass fraction sensors. These sensors include real time Optical Particle Counters that utilize a laser to count and size particles into eight user-specified size bins (OPC Model 9722, Met One Instruments, Inc., Grants Pass, OR). The aerodynamic particulate impactors are portable, self-contained, filter-based particulate samplers containing Teflon filters that are weighed pre- and post-exposure (MiniVol, Airmetrics, Eugene, OR.) By co-locating AirMetric samplers and OPC instruments, we established the relationship between mass concentration and aerosol backscatter. Aerosol parameters are developed for lidar characterization and calibration by directing the lidar beam past the AirMetric/OPC instrument pair [35].

Observations performed with the Aglite system reveal that the measurements are distributed as Poisson-distributed random variables. Fig. 3A shows data from a 6-minute time span with Aglite staring continuously in one direction through the atmosphere. These data were taken from an almond orchard, where Aglite observed a harvesting operation. Ensemble averages and variances were calculated for each range over varying period lengths. Fig. 3B and C illustrate the relationships between estimated average power and variance of the lidar signal as a function of ensemble period for the range of 780 m. Fig. 3B, C, and D all describe data taken over a 14-minute interval from a campaign at a cotton gin. Fig. 3B shows the relationship of ensemble averaged mean power and variance to ensemble period. The relationship between ensemble averaged mean power and variance at all ranges for the 100-second ensemble period is shown in Fig. 3C. A particle normalized histogram of the measured lidar signal at 780 m is compared to Poisson distributions in Fig. 3D. The main source of noise in Aglite data is photon-counting noise. Background solar radiation also contributes significantly to the signal, which increases the total number of photons measured by the detectors and hence increases the noise in the signal.

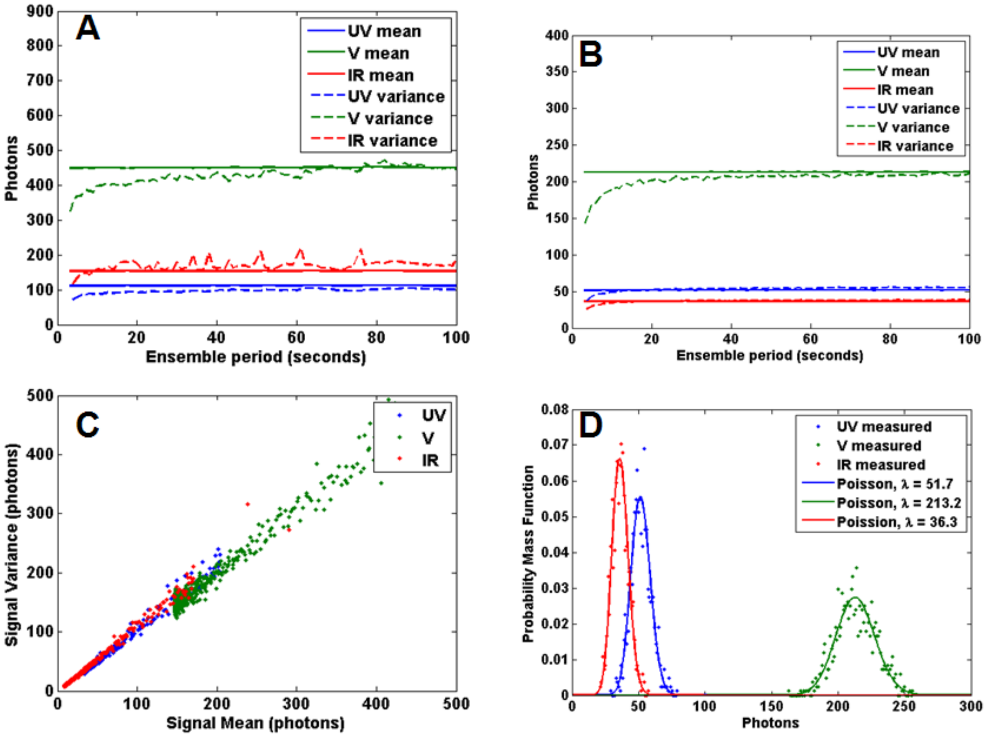

Fig. 3. (A) 6-minute continuous stare taken during an almond harvesting operation. (B) Average power and variance of the lidar signal as a function of ensemble period for data taken at 780 m. (C) Relationship between average power and variance of the lidar signal. (D) A comparison between a photon-normalized histogram of Aglite measurements against a Poisson probability mass function.

Representative plots of the signal-to-noise ratio (SNR) of the retrieved backscatter for each of the three wavelengths as a function of distance are shown below. In this case, SNR is defined as the ratio of the mean aerosol backscatter amplitude over the standard-deviation of the aerosol backscatter. Fig. 4A shows the SNR measured from data taken during an almond harvest. For this measurement, the laser output power was attenuated to 20% of full power for reasons of eye-safety, and the PM_{10} level was approximately 13 $\mu g/m^3$. Fig. 4B shows the SNR measured at a cotton gin operation. In this case, the laser was unattenuated, and the background levels of PM_{10} were approximately 25 $\mu g/m^3$. These plots cannot be directly compared to each other because of the many possible differences in aerosol loading, aerosol type, and meteorological conditions, as well as output power differences; however, these plots do illustrate realistic SNR values for Aglite in field conditions. The dips in the plots of Fig. 4A and B are due to the environmental variability of the emission aerosols at the site. Smooth portions of the plots correspond to homogeneous regions of atmosphere.

For these measurements, in-situ instruments were used to absolutely calibrate the lidar signal and to determine the ratio of the aerosol backscatter contribution to the backscatter contribution due to molecular scattering. The SNR at a given range can be improved either by not attenuating the laser, or by increasing the integration time of the measurement. SNR of the visible beam is lower in Fig. 4A (daylight) than in Fig. 4B (night) due to solar intrusion.

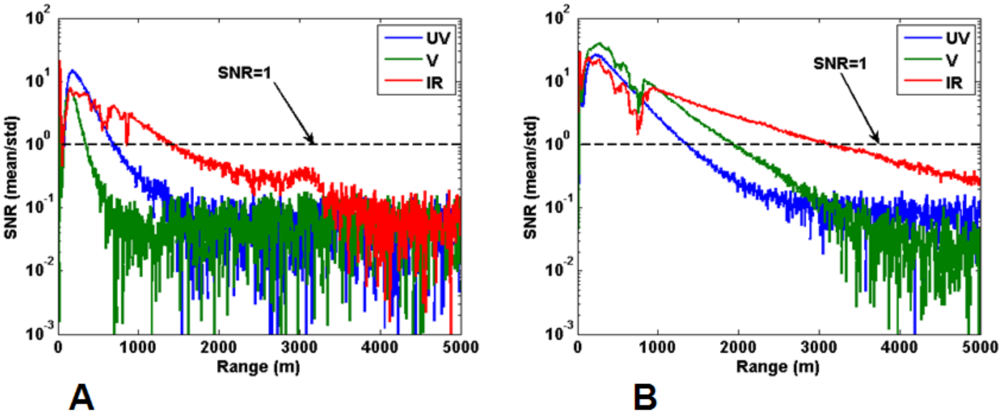

Fig. 4. Two examples of SNR values observed by Aglite under field conditions for (A) an almond nut harvest and (B) a cotton gin operation. SNR is a function of range, output power, aerosol loading, and solar background illumination.

4 EXAMPLE DATA AND DISCUSSION

The Aglite system has been deployed at several agricultural facilities in the U.S. since becoming operational in the summer of 2005. Examples from these campaigns are given below to illustrate Aglite's ability to capture the structure and dynamics of plumes from agricultural sources.

4.1 Aerosol Detection Capability

The lidar control computer has the useful ability to display the raw lidar signal in real time (Fig. 5A). This allows the individual wavelength return signals to be monitored so that the data integration time can be adjusted and pulse dead-time corrections can be made as needed. The control computer also stores the raw lidar signal for later processing.

Additionally, the lidar includes a display unit which shows 2-D images of the lidar scan regions in near real time. This display removes the DC component of the background noise and performs range-correction to the signal amplitude before displaying the data. The conversion of raw lidar data into aerosol concentration is performed after the conclusion of a campaign.

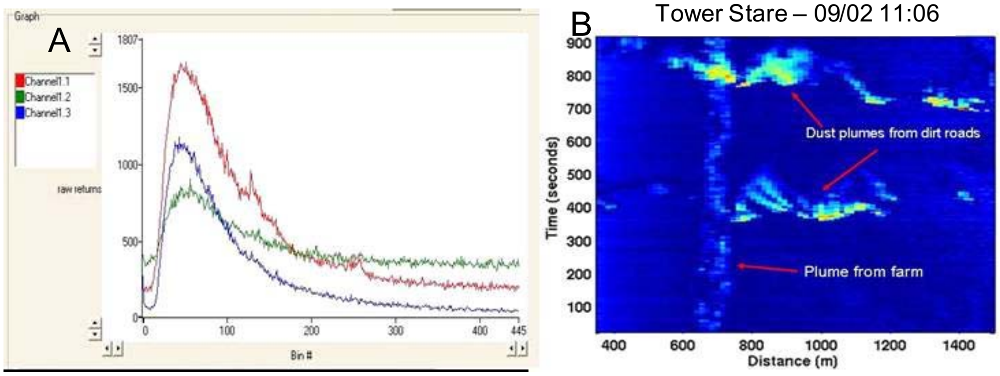

Fig. 5. (A) Monitor photograph of the raw lidar scan, showing the return strength of the 3 wavelengths (red = IR, green = visible, blue = UV) as a function of range bin (6 m). (B) Range corrected IR return intensity as a function of time with the lidar staring past a tower mid facility.

The Aglite software consists of three parts: the lidar control software, the visualization software, and the lidar retrieval software. The lidar control software governs the data acquisition and pointing control of the lidar hardware. This program is written in the Labview programming environment and is installed on the PC in the Aglite hardware rack. The main functions of this program are to control the pointing of the steering mirror and store the values measured by the photon detectors. The software allows the user to control the lidar either manually, by means of a game controller, or in an automatic mode, in which the program directs the lidar scan in a repeating predetermined pattern. This program also controls parameters such as the PMT voltage levels, the range gate, and the integration time of the lidar. This program writes the lidar measurements and orientation parameters to a data file for storage and also broadcasts them over the local computer network using the UDP protocol. This program graphs in real time the current raw signal measured by Aglite.

The visualization software is a program with a graphical user interface written in the Matlab programming environment. The function of this program is to assist the operator by providing real-time visualization of lidar data. The visualization software is installed on a separate laptop that is networked to the rack-mounted PC. The visualization software captures the data broadcast by the rack-mounted PC broadcasts and plots them in range-normalized form. The user selects the range and channel of data to view. The visualization software automatically determines the type of motion currently being performed—stare, horizontal sweep, or vertical sweep—and plots it in an appropriate 2-D graph. The visualization software is also able to plot data from the archived data files generated by the lidar control software.

The lidar retrieval software consists of a set of scripts written for the Matlab programming environment. The lidar retrieval software retrieves PM concentration from the lidar data files, allowing the lidar scans to be converted into maps of aerosol concentration. An aerosol may scatter the three wavelengths of Aglite with different efficiencies. This allows the retrieval software to extract information about the aerosol particle size distribution as well as the concentration of the aerosol. This software does not run concurrently while the lidar is taking data, but is executed offline, after the measurements have been completed. This software requires additional inputs from point sensors to calibrate the lidar signal and to calculate the lidar-ratio and other parameters needed to perform the lidar retrieval. The retrieval algorithm of the lidar retrieval software is described in detail by Zavyalov et al. [35].

4.1.1 Fixed Lidar Direction

Fig. 5B shows data collected during a lidar "stare" period in which the FOV is fixed horizontally so the lidar can record the range-dependent backscatter as a function of time (here about 15 minutes). These measurements are from a field-campaign at a swine-finishing facility. This stationary stare past a barn complex shows an emission plume from the facility (~ 650m) and two transient road dust plumes. The co-location of the lidar path and the tower-mounted particle monitors close to the barns provides the essential step for the optical-particulate calibration of the lidar.

The choice to design Aglite with three channels adds significant cost and complexity over a one-channel design. The additional channels, however, provide additional information about the aerosol characteristics under investigation. The point sensors deployed with Agite directly measure the particle size distribution of both the background atmosphere aerosol and the target aerosol under investigation. The accuracy of these point measurements can be gauged by comparing them to Aglite measurements.

An example is given here of retrieving aerosol concentration and mode radius using Aglite's lidar retrieval algorithm. A stationary stare past the barn complex was performed for 400 seconds and averaged. This measurement was pre-processed to remove the DC noise component and to correct for the GFF. The measurement was then converted to the logarithmic range-normalized form, as shown in Fig. 6A. The lidar inversion was performed using the Klett solution for two scatterers. This is illustrated in Fig. 6B.

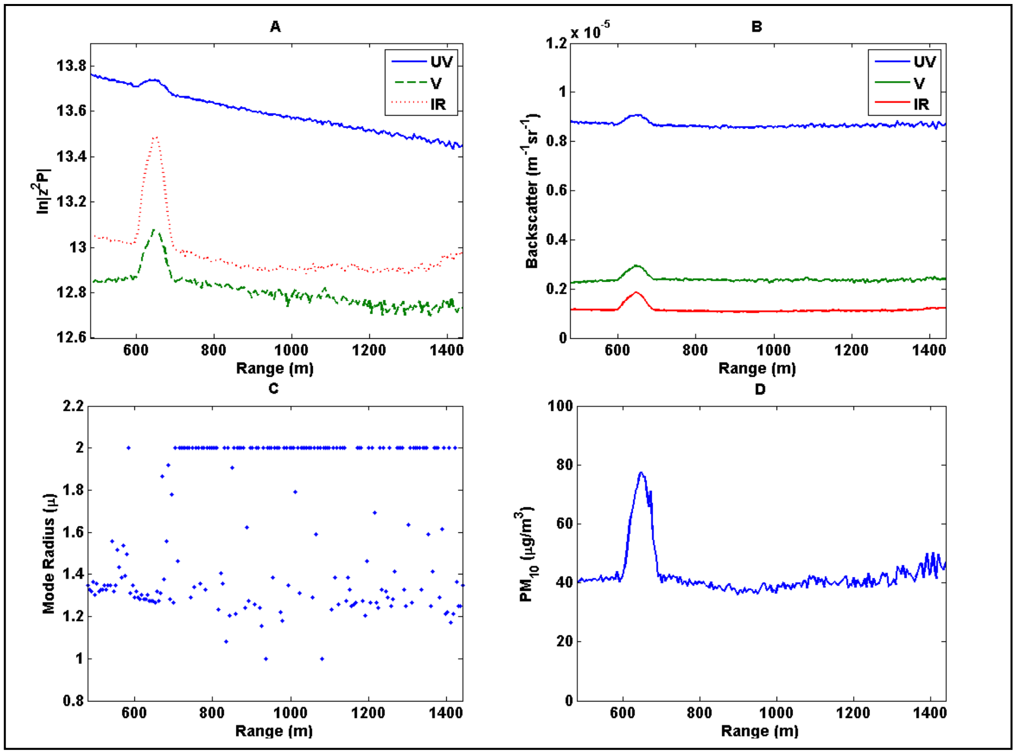

Fig. 6. (A) A 400-second stationary stare past a swine barn complex, in logarithmic range-normalized form. (B) Backscatter values retrieved from the same measurement. (C) The mode-radius values of the least-squares solution. (D) The PM_{10} concentration values given by the solution.

Point sensor measurements were used to provide the backscatter values of the homogeneous background and the lidar ratios for the two scatterers. A least-squares solution for aerosol concentration and mode radius was then calculated at every range, assuming a log-normal distribution with σ=2.0 and indices of refraction for a water-soluble aerosol [38]. The retrieved mode-radius as a function of range is given in Fig. 6C. The solution for mode radius was restricted to a window between 1 and 2 microns. It reasonable to assume that when the solution to the mode radius was at the limits of this window, there may have been insufficient aerosol to accurately measure the mode radius. This is supported by the fact that at ranges where a plume is visible in Fig. 6B, the retrieved mode radius is comfortably within the allowable window of values. Fig. 6D shows the PM_{10} concentration that results from the solution, assuming unit density. A complete description of the algorithm is given elsewhere [35], along with details of the algorithm's performance and more examples of its use.

4.1.2 Crosswind scans for aerosol flux measurements: "Staple" scans

The lidar scan patterns typically used to characterize the amount of aerosol emissions include vertical profiles between barns at upwind and downwind facility boundaries and horizontal profiles above the facility. Interleaved with these scans of the facility area are stationary stares near the in situ instruments to probe the aerosol parameters.

Fig. 7A illustrates the use of horizontal scans that serve to locate the sources of aerosol emissions around an agricultural facility. These scans are particularly useful when placing the aerosol point sampling equipment. While even a single wavelength system can provide these types of data, the multiple wavelength capability of Aglite comes into play in determining and tracking the distribution of particulate size classes and their flux from the facility.

Fig. 7B introduces a type of scan called a "staple" scan, which Aglite uses extensively to bracket the net emission from an agricultural facility [26]. The range dependent lidar signal is displayed in false color in three steps: an elevation scan upwards, an azimuthal scan to the right, and an elevation scan downwards. Here the wind blows from right to left. On the left side, the lidar captures plumes generated by traffic on an adjacent gravel road at distances between 1 and 3 km that have risen to almost 300 meters altitude. Next, the horizontal scan encounters plume material that has risen to a higher altitude as the plume is transported downwind. Lastly the downward elevation scan on the right displays the fully developed plume portions that have blown away from the lidar to a range of about 5 km. Each scan can be completed in 1-1.5 minutes, depending on the background aerosol intensity and desired SNR.

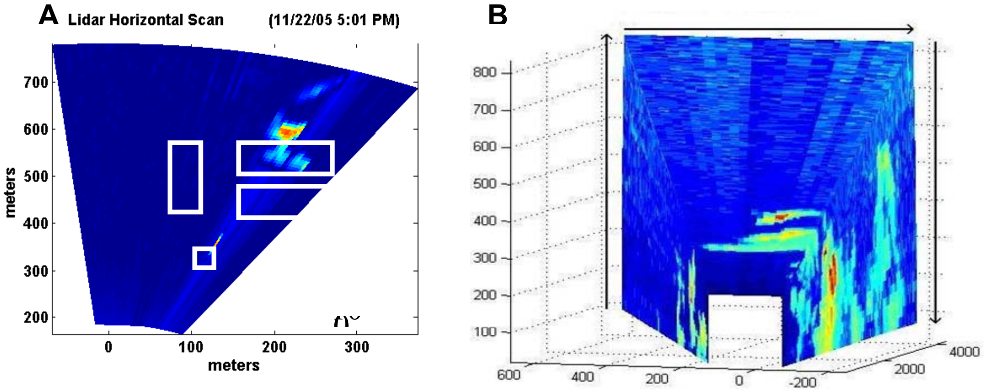

Fig. 7. (A) Typical Aglite horizontal scan for locating aerosol sources within a facility. (B) A "staple" scan showing plume material dispersing as it moves to the right and rises above horizontal the lidar scan plane.

4.2 Aerosol Traced Wind Motion

4.2.1 Wind Velocity from Lidar "Stares"

Fig. 8 shows aerosol return data collected with the beam parallel to a graveled road in a fixed, horizontal stare. Each strong signal return represents a dust cloud generated by a road traffic event. Direction motion of aerosols is towards the lidar, with a dashed line tracking the movement of individual return features over time. The figure shows distance from the lidar on the horizontal axis and time difference on the vertical access. Tracking such long plume trains is possible because the lidar can see through individual plumes that have very low aerosol density and optical extinction. The color scale represents the lidar signal intensity from blue (weak) to red-orange (strong). As in Fig. 5B, this display is a space-time (x, t) graph of plume motion, with time increasing upward and lidar range increasing to the right. This type of lidar data record and subsequent velocity analysis is analogous to "streak photography," which has found wide applications in experimental fluid dynamics [39][40][41][42]. Holmén, Eichinger and Flocchini (1998) and Holmén et al. (2001) adopted this method for lidar and pointed out its significance for quantitatively measuring plume velocity and transport based on straightforward physical calibrations of distance and time [6][7].

In Fig. 8, the wind motion is from right to left and, based on the persistence of the x-t streaks, lies directly within the lidar field of view. When the lidar is not aligned with the wind direction, the streaks are much shorter, as the cloud moves across the beam. The slopes of these aerosol traces (dashed lines) are direct measures of the wind speed (distance/time). The speed observed in this figure is consistent with the data measured on a tower at the 600 m range. As expected, the wind also demonstrates velocity variations with distance (shown in the white boxes). The lidar is so sensitive that clumps and clouds of aerosols can be tracked in daytime and nighttime situations, even when they are too tenuous to be seen by eye.

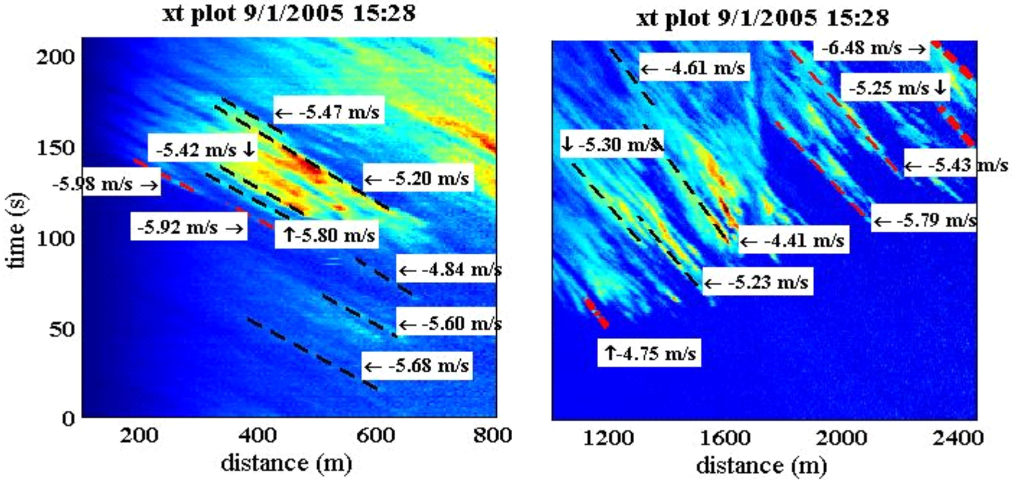

Fig. 8. Local wind patterns shown in time series of lidar returns at different lidar ranges. Aerosol plume velocities shown are measured directly from the slopes of the plume traces.

Most of our "staring" observations have been made at reasonably steady winds above 3 m/sec. During one of our experiments, we observed one noteworthy occasion of very slow and highly variable horizontal air motion at the 20-m height. This state of motion suggests almost stagnant air dominated by convection with a fluctuating horizontal wind component. This is shown in Fig. 9 where the horizontal speeds varied between 1.4 m/sec toward the lidar and 1.5 m/sec away from the lidar, out to a range of 5 km. In addition to the well-defined parts of the plumes, there are low-contrast, triangular patches in this x-t image indicating that a 1-1.5 km-wide pattern of drifting motion of aerosols persisted for at least 5 minutes. This is a remarkable cross-sectional snapshot of an atmospheric pattern that could not be seen by any means other than lidar. The capability of lidar as a tool for documenting wide area patterns of air motion dominated by convection is an important addition to the study of aerosol transport from agricultural sources.

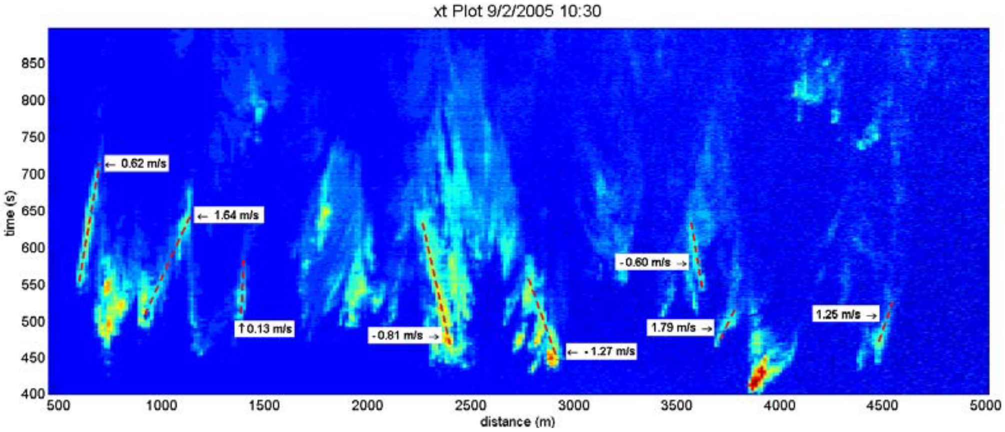

Fig. 9. Returns from an eight-minute horizontal stare @ 20m height during light and variable wind conditions. Air motion toward and away from the lidar is indicated by the varied slopes of the individual aerosol clumps (radial velocity is shown in the white boxes).

4.2.2 Vertical Scans for Cross-Sections of Moving Plumes

The staring and staple scans with the lidar show that the aerosol transport consists of clumps of highly variable particle concentrations that originated from ground level. To see the full structure and height of these plumes and how they evolve, one must use vertical lidar scans $\theta(t) = \theta_0 \pm Ct$ aimed upwind or downwind, with the scans made rapidly enough to follow the plume propagation over a range of hundreds of meters. These scans can display complete cross sections of plume structure as opposed to accidental intersections orthogonal to the motion. For the data shown in Fig. 10, the lidar alternately scanned up and down at a rate of $C = 0.1°/s$. The resulting images are divided into interleaved sequences of "up" frames and "down" frames. Each sequence shows radial aerosol plume motion with the wind towards the lidar. Each panel was recorded over a 30-second vertical scan. This record of plume motion shows a total of 4 minutes of aerosol transport of road dust plumes.

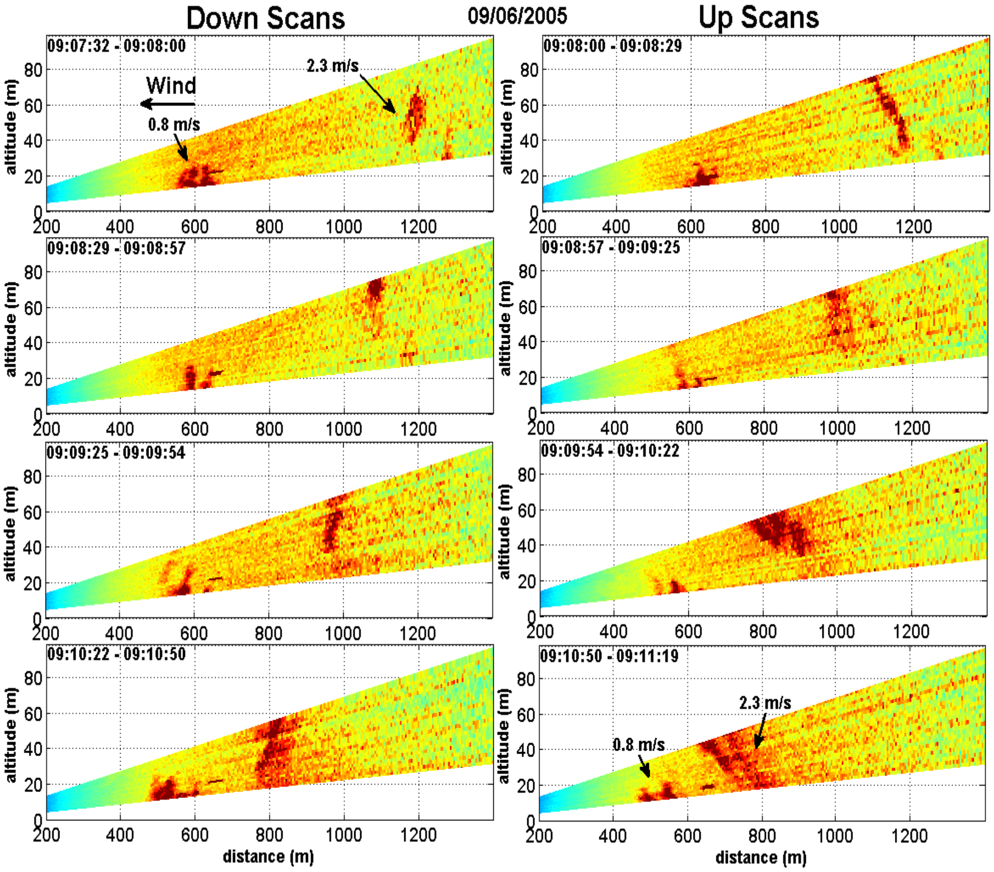

Fig. 10. A series of 30-second vertical scans (four minutes total) of plumes moving toward the lidar. Speeds of two plume groups differ by a factor of 3.

Two distinct plume populations are evident in Fig. 10: (1) low-altitude, low-velocity (0.8 m/s) plumes originating at 600 m, and (2) higher plumes with higher speeds (2.3 m/s) that originate from more distant sources. The visualization of these structures provides important information regarding the scales of aerosol inhomogeneities involved in particle transport.

There are obvious differences between up and down images due to the kinematic distortion inherent in the record of a moving object (plume) obtained by the time-dependent scan *θ(t)*. These images show that a plume's true shape and velocity can be reconstructed assuming the linear time dependence of the angular scan cited previously. The images also show that many plumes, while ragged, are fairly straight pillars that tilt substantially forward from vertical by 40º – 45º in the wind direction, as described by Stull [43], Kaimal and Businger [44], Wilczak and Tillman [45], and Wilczak [46]. Laboratory observations of such fluid flows were shown by Prandtl [47]. Instability in the atmospheric surface layer produces intermittent gusts in which the local vertical velocity can be comparable to the horizontal wind, creating a plume of soil aerosols carried upward at an angle tilted nearly 45º forward in the wind direction.

To demonstrate unscrambling the simultaneous time dependence of lidar scans and plume motions, we include in Fig. 11 a graphic representation of simulations developed for plume analysis. The tilted plume is represented initially by the heavy black line and later by a series of parallel dashed lines as the plume blows to the left. As the moving plume is intercepted by the lidar scan, the intersection first rises (left panel) in an arc from **A** to **B,** and then connects to a down-going arc from **B** to **C** (right panel). The velocity and forward tilt calculated for this plume are unique solutions to the kinematic equations underlying these arcs. The forward/backward tilts in the scans serve as signatures for radial plume motions of the wind speed component along the line of sight of the lidar.

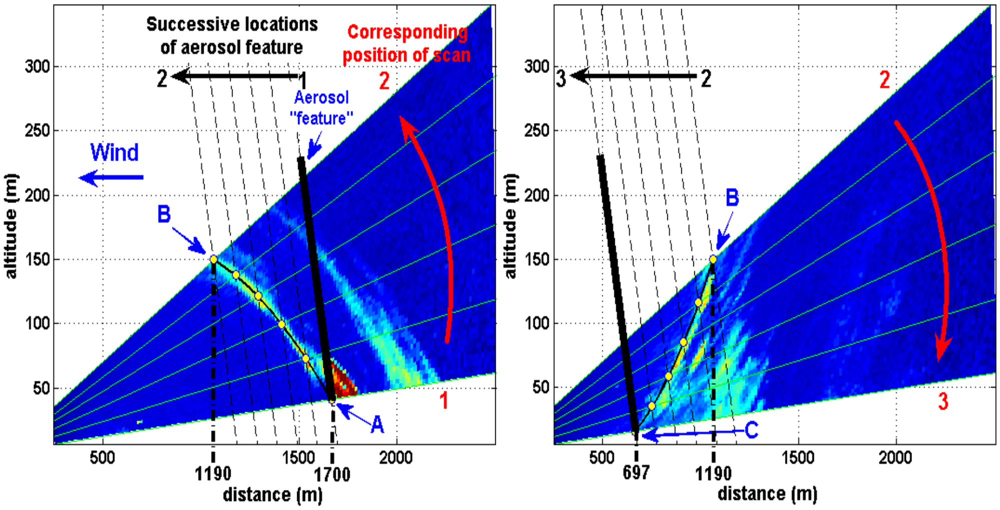

Fig. 11. Scan velocity correction for the distorted patterns of an aerosol plume blowing toward the lidar at 4 m/s. Scan direction is up (left) and down (right). Note the relative scales of the axes: the plume is actually tilted 40°forward from vertical.

The observational value and advantage of lidar, as illustrated here, is that it clearly provides an extremely sensitive way to see tenuous aerosol features that are hard to see or photograph. We were unable to obtain conventional pictures of the above plumes because of low optical contrast. However, we made a successful attempt to photograph such plumes elsewhere under more extreme conditions. We sought an environment where wind, surface temperature, lighting, and loose dust could make it possible to obtain visible images of plumes. Fig. 12 is a photograph taken in the Black Rock desert in Nevada in September 2006. Similarly to the lidar observations, these plumes retained shape as they marched steadily to the east with the wind, and were tilted substantially forward at near -45º angles that varied slightly during any single gust event.

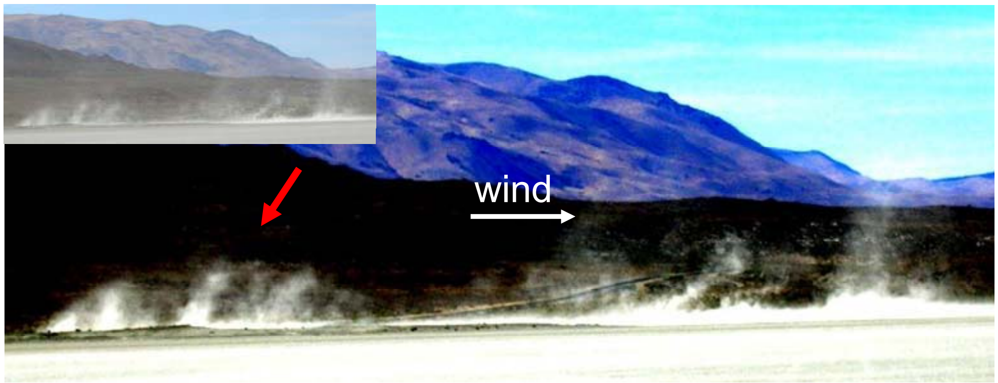

Fig. 12. Wind-blown plumes of clay dust in Nevada. Plumes are tilted forward in the wind.

5 CONCLUSION

The Aglite lidar was developed to provide a tool for rapidly characterizing agricultural and other anthropogenic aerosol sources. It has normally been deployed as a member of a suite of classical aerosol characterization instruments that provide the additional aerosol optical response functions required to fully understand the sources and their emission rates. The lidar beam can be scanned in the horizontal and vertical planes to allow emission tracking and profiling. The lidar allows the mapping the relative backscatter of an aerosol plume at 1064, 532, and 355 nm wavelengths, with a resolution of 12 meters (range) and 5 milliradians (angle). Sensitivity at up to 10 samples/second is sufficient to identify non-visible facility plumes of US EPA-regulated PM_{10} and $PM_{2.5}$ particulates.

The lidar has been used to create near real time profiles of plume structures and low-elevation clouds and to map the location of aerosol sources over a range of facility types, including a confined agricultural feeding operations, agricultural product processing, and mobile source operations where variable wind and short-duration treatment evaluations are desired. Processing the lidar returns also allow the wind speed and the character of the temporal and spatial variation of aerosol plume structures to be determined.

When the lidar is combined with point instruments to provide the additional aerosol characteristics to determine optical parameters, the system can provide calibrated aerosol fraction information and emission fluxes from the studied operations [35]. The most important capabilities for Aglite's monitoring of agricultural emissions are (1) the mapping of aerosol concentration and motion around a facility and (2) the measurement of absolute aerosol mass concentration emission of a facility.

ACKNOWLEDGEMENTS

The development of the Aglite system was performed under USDA Agreement number 58-3625-4-121 with Dr. Jerry Hatfield, the Director of the National Soil Tilth Laboratory in Ames, Iowa, providing valuable direction to the Aglite development team. Any opinions, findings, conclusions, or recommendations expressed in this publication are those of the authors and do not necessarily reflect the view of the USDA. The authors also acknowledge Dr. Michael D. Wojcik of SDL for providing valuable suggestions on the manuscript.

REFERENCES

[1] "40 CFR 50.6—National primary and secondary ambient air quality standards forPM10," Code of Federal Regulations—Title 40: Protection of Environment (2005) http://vlex.com/vid/19784798.

[2] "40 CFR 50.7—National primary and secondary ambient air quality standards for PM2.5," Code of Federal Regulations—Title 40: Protection of Environment (2005) http://vlex.com/vid/19784804.

[3] J. B. Baker, R. J. Southard, and J. P. Mitchell, "Agricultural dust production in standard and conservation tillage systems in the San Joaquin Valley," J. Environ. Quality 34, 1260-1269 (2005) [doi:10.2134/jeq2003.0348].

[4] H. Clausnitzer and M. J. Singer, "Respirable-dust production from agricultural operations in the Sacramento Valley, CA," J. Environ. Quality 25, 877-884 (1996).

[5] H. Clausnitzer and M. J. Singer, "Intensive land preparation emits respirable dust," J. California Agri. 51, 27-30 (1997).

[6] B. A. Holmén, W. E. Eichinger, and R. G. Flocchini, "Application of elastic lidar to PM10 emissions from agricultural nonpoint sources," Environ. Sci. Technol. 32(20), 3068-3076 (1998) [doi:10.1021/es980176p].

[7] B. A. Holmén, T. A. James, L. L. Ashbaugh, and R. G. Flocchini, "Lidar-assisted measurement of PM10 from agricultural tilling in California's San Joaquin Valley-

Part I: lidar," Atmos. Environ. 35(19), 3251-3264 (2001) [doi:10.1016/S13522310(00)00518-5].

[8] B. A. Holmén, T. A. James, L. L. Ashbaugh, and R. G. Flocchini, "Lidar-assisted measurement of PM10 from agricultural tilling in California's San Joaquin Valley Part II: emission factors," Atmos. Environ. 35(19), 3265-3277 (2001) [doi:10.1016/S1352-2310(00)00519-7].

[9] B. Holmen, D. Miller, A. Hiscox, W. Yang, T. Sammis, and R. Bottoms, "Nearsource particulate emissions and plume dynamics from agricultural field operations," J. Atmos. Chem. 59(2), 117-134 (2008) [doi:10.1007/s10874-007-9086-6].

[10] A. L. Hiscox, D. R. Miller, B. A. Holmen, W. Yang, and J. Wang, "Near-field dust exposure from cotton field tilling and harvesting," J. Env. Quality 37, 551-556 (2008) [doi:10.2134/jeq2006.0408].

[11] W. T. Buttler, C. Soriano, J. M. Baldasano, and G. H. Nickel, "Remote sensing of three-dimensional winds with elastic lidar: explanation of maximum crosscorrelation method," Boundary-Layer Meteor. 101(3), 305-328 (2001) [doi:10.1023/A:1019274424820].

[12] V. A. Kovalev and W. E. Eichinger, ElasticLidar: Theory, Practice, and Analysis Methods, Wiley-Interscience, Hoboken, NJ. (2004).

[13] V. E. Derr and C. G. Little, "A comparison of remote sensing of the clear atmosphere by optical, radio, and acoustic radar techniques," Appl. Opt. 99, 1982-1983 (1970).

[14] V. E. Zuev, "Lidar sounding of the atmosphere to estimate static and dynamic characteristics of aerosol inhomogeneities," Proc. 5th Conf. Laser Radar Studies of the Atmosphere, pp.104-105 (1973).

[15] E. W. Eloranta, J. M. King, and J. A. Weinman, "The determination of wind speeds in the boundary layer by monostatic lidar," J. Appl. Meteorol. 14(18), 1485-1489 (1975) [doi:10.1175/1520450(1975)014<1485:TDOWSI>2.0.CO;2].

[16] Y. Sasano, H. Hirohara, T. Yamasaki, H. Shimizu, N. Takeuchi, and T. Kawamura, "Horizontal wind vector determination from the displacement of aerosol distribution patterns observed by a scanning lidar," J. Appl. Meteor. 21(10), 1516-1523 (1982) [doi:10.1175/15200450(1982)021<1516:HWVDFT>2.0.CO;2].

[17] W. P. Hooper and E. W. Eloranta, "Lidar measurements of wind in the planetary boundary layer: the method, accuracy, and results from joint measurements with radiosonde and kytoon," J. Clim. Appl. Meteorol. 25(7), 990-1001 (1986) [doi:10.1175/1520-0450(1986)025<0990:LMOWIT>2.0.CO;2].

[18] D. I. Cooper and W. E. Eichinger, "Structure of the atmosphere in an urban planetary boundary layer from lidar and radiosonde observations," J. Geophys. Res. 99, 22937- 22948 (1994) [doi:10.1029/94JD01944].

[19] P. W. Young and E. W. Eloranta, "Calculation of divergence and vertical motion from volume imaging lidar data," J. Geophys. Res. 100, 25557- 25583 (1995) [doi:10.1029/94JD03119].

[20] W. E. Eichinger, D. I. Cooper, J. L. Hatfield, L. E. Hipps, J. J. Nicholls, R. L. Pfeiffer, and J.H. Preuger, "Use of elastic lidar to examine the dynamics of plume dispersion from an agricultural facility," presented at Workshop on Agricultural Air Quality: State of the Science, Ecological Society of America, pp. 215-226 (June 4-8, 2006).

[21] G. K. Schwemmer, Conically Scanned Holographic Lidar Telescope, U.S. Patent No. 5,255,065 (1993).

[22] D. V. Guerra, G. K. Schwemmer, A. D. Wooten Jr., S. S. Chaudhuri, and T. D. Wilkerson, "Prototype holographic atmospheric scanner for environmental remote

sensing," J. Geophys. Res. 104(D18), 22287-22292 (1999) [doi:10.1029/1999JD900324].

[23] G. K. Schwemmer, T. D. Wilkerson, J. A. Sanders, D. V. Guerra, D. O. Miller, and S. E. Moody, "Ground based operational testing of holographic scanning lidars," in Advances in Laser Remote Sensing, A. Dabas, C. Loth, J. Pelon, Eds., pp. 69-72, Ecole Polytechnique, France (2001).

[24] T. D. Wilkerson, J. A. Sanders, and I. Q. Andrus, Kinematic Analysis of Conically Scanned Environmental Properties, U.S. Patent No. 6, 535, 158 (2003).

[25] T. D. Wilkerson, S. Cornelsen, C. Earl, D. Huish, J. Cutts, S. Call, M. Anderson, and G. K. Schwemmer, "Monitoring of air motion using lidar and video observations," Proc. Am. Meteor. Society. 2nd Symp.Lidar Atmospheric Applications (2005) http://ams.confex.com/ams/pdfpapers/84891.pdf.

[26] G. E. Bingham, C. C. Marchant, V. V. Zavyalov, D. J. Ahlstrom, K. D. Moore, D. S. Jones, T. D. Wilkerson, L. E. Hipps, R. S. Martin, J. L. Hatfield, J. H. Prueger, and R. L. Pfeiffer, "Lidar based emissions measurement at the whole facility scale: Method and error analysis," J. Appl. Rem. Sens., under review (2009).

[27] M. McGill, D. Hlavka, W. Hart, V. S. Scott, J. Spinhirne, and B. Schmid, "Cloud physics lidar: instrument description and initial measurement results," Appl. Opt. 41(18), 3725-3734 (2002) [doi:10.1364/AO.41.003725].

[28] R. Agishev, B. Gross, F. Moshary, A. Gilerson, and S. Ahmed, "Simple approach to predict APD/PMT lidar detector performance under sky background using dimensionless parametrization," Optics and Lasers in Eng. 44(8), 779-796 (2006) [doi:10.1016/j.optlaseng.2005.07.010].

[29] S. Cornelsen, "Electronics Design of the AGLITE Instrument," MS Thesis, Utah State University (2005).

[30] W. Gong, T. H. Chyba, and D. A. Temple, "Eye-safe compact scanning LIDAR technology," Optic. Laser. Eng. 45(8), 898-906 (2007) [doi:10.1016/j.optlaseng.2007.01.008].

[31] "American National Standard for the Safe Use of Lasers," Z136.1, Laser Institute of America, ANSI, New York (2000).

[32] F. C. Delori, R. H. Webb, and D. H. Sliney, "Maximum permissible exposures for ocular safety (ANSI 2000), with emphasis on ophthalmic devices," J. Opt. Soc. Am. A 24(5), 1250-1265 (2007) [doi:10.1364/JOSAA.24.001250].

[33] R. Baxter, "Laser safety training manual," Univ. Chicago Chemistry Dept. (2001) http://chemistry.uchicago.edu/safety/LaserSafety.pdf.

[34] A. L. Augustoni, "Laser hazard analysis for airborne AURA (Big Sky Variant) Proteus platform," SAND2004-0413, Sandia National Laboratories (2004).

[35] V. V. Zavyalov, C. C. Marchant, G. E. Bingham, T. D. Wilkerson, J. L. Hatfield, R. S. Martin, P. J. Silva, K. D. Moore, J. Swasey, D. J. Ahlstrom, and T. L. Jones. "Aglite lidar: calibration and retrievals of well characterized aerosols from agricultural operations using a three-wavelength elastic lidar," J. Appl. Rem. Sens., under review (2009).

[36] R. M. Measures, Laser Remote Sensing: Fundamentals and Applications, John Wiley, Inc., New York (1984).

[37] S. W. Dho, Y. J. Park, and H. J. Kong, "Experimental determination of a geometrical form factor in a lidar equation for an inhomogeneous atmosphere," Appl. Opt. 36(24), 6009-6010 (1997) [doi:10.1364/AO.36.006009].

[38] A. S. Jursa, Handbook of Geophysics and the Space Environment, Air Force Geophysics Lab. (1985).

[39] E. Mallard and H. L. Le Chatelier, Comptes Rendu 93, 145 (1881).

[40] H. B. Dixon, "On the movement of the flame in the explosions of gases," Phil. Trans. Roy. Soc. A200, 315-352 (1903).

[41] B. Lewis and G. von Elbe, Combustion, Flames and Explosions of Gases, Academic Press, Inc. (1951).

[42] O. Laporte and T. D. Wilkerson, "Hydrodynamic aspects of shock tube spectroscopy," J. Opt. Soc. Am. 50(12), 1293-1299 (1960) [doi:10.1364/JOSA.50.001293].

[43] R. B. Stull, An Introduction to Boundary Layer Meteorology, pp. 441-450, Kluwer Academic Publishers, Netherlands (1998).

[44] J. C. Kaimal and J. A. Businger, "Case studies of a convective plume and a dust devil," J. Appl. Meteorol. 9(4), 612-620 (1970) [doi:10.1175/15200450(1970)009<0612:CSOACP>2.0.CO;2].

[45] J. M. Wilczak and J. E. Tillman, "The three-dimensional structure of convection in the atmospheric surface layer," J. Atmos. Sci. 37(11), 2424-2443 (1980) [doi:10.1175/15200469(1980)037<2424:TTDSOC>2.0.CO;2].

[46] J. M. Wilczak and J. A. Businger, "Thermally indirect motions in the convective atmospheric boundary layer," J. Atmos. Sci. 40(2), 343-358 (1984) [doi:10.1175/15200469(1983)040<0343:TIMITC>2.0.CO;2].

[47] L. Prandtl, Führer durch die Strömungslehre, 3rd ed., F. Vieweg and Sohn, Braunschweig (1942).